Effect of structural disordering on magnetic and magneto-optical properties of Fe$_3$Si

B. H. Zhang,[1] Z. Wang,[1] Y. N. Zhang,[2,*] and R. Q. Wu [3,†]

[1]*State Key Laboratory of Surface Physics, Key Laboratory of Computational Physical Sciences,*
and Department of Physics, Fudan University, Shanghai 200433, China
[2]*Institute of Fundamental and Frontier Sciences, University of Electronic Science and Technology of China, Chengdu 611731, China*
[3]*Department of Physics and Astronomy, University of California, Irvine, California 92697, USA*

The electronic, magnetic, transport, and magneto-optical properties of the $D0_3$ and amorphous Fe$_3$Si are investigated by using the first-principles calculations. A strong correlation between local magnetization and atomic arrangement is established. The amorphization significantly alters the spin polarization and the magneto-optical Kerr rotation spectrum but has a little influence on anomalous Hall conductivity. Analyses in band structures and interband matrix elements provide clear insights for the understanding of these results.

I. INTRODUCTION

Iron silicides provide rich electronic properties for fundamental studies as well as for diverse applications such as in optoelectronic, thermoelectric, and spintronic devices [1–10]. For instance, the Si-rich β-FeSi$_2$ is a semiconductor with a band gap of about 0.87 eV, making it suitable for the use in optoelectronic technologies [1–3]. On the Fe-rich side, Fe$_5$Si$_3$ [7] and Fe$_3$Si [8–10] are metallic ferromagnets at room temperature, and hence are promising as efficient spin-injection sources in spintronic and magnetic devices. The bulk Fe$_3$Si is a Heusler alloy with a high Curie temperature ($\approx$803 K) [8], as well as a relatively large spin polarization at the Fermi level ($\approx$43%) [11]. In particular, it is almost perfectly lattice matched with the GaAs(001) substrate, allowing high-quality epitaxial growth with atomically flat interfaces, a desired feature for achieving high spin-injection rate. Indeed, Herfort *et al.* have recently reported epitaxial growth of Fe$_3$Si layers on GaAs(001) with a sharp interfacial perfection [12], and they successfully realized spin injection from Fe$_3$Si into GaAs at room temperature [13]. Many studies have been carried out afterwards on growing Fe$_3$Si layers on various semiconductor substrates, including Si [14–16], Ge [17,18], and MgO. [19,20] A variety of attractive phenomena has been discovered such as the Fermi-level pinning [21], the tunneling magnetoresistance effect [22], large magnetic anisotropy [19,23–25], and planar Hall effect [26–28].

Crystalline Fe$_3$Si is known to have multiple local structures and thus can accommodate substitutional transition-metal impurities [29]. It is believed that the spintronic properties of Fe$_3$Si systems can be improved or modified by changing their atomic arrangements. Recently, by introducing a certain amount of Mn atoms into Fe$_3$Si, Hamaya *et al.* showed that it is possible to get a high spin polarization of $P \geqslant 0.9$ in Fe$_{3-x}$Mn$_x$Si/Ge(111) at room temperature when $x \approx 0.6$. Lattice strains can also have a significant influence on the electronic and transport properties of Fe$_3$Si films [30]. Zhang *et al.* investigated the strain effect on the magnetic anisotropy energies of epitaxial Fe$_3$Si and nonstoichiometric Fe$_{100-x}$Si$_x$($x = 6.25{\sim}25$) films on the MgO(001) substrate [25], and found that the magnetic easy axis can be changed from the in-plane direction to the out-of-plane direction by applying an appropriate compressive vertical strain. Structural disordering is also an important mean to tune the magnetic and electronic properties. While the epitaxial Fe$_x$Si$_{1-x}$ ($0.5 < x < 1.0$) films mostly have the $D0_3$ or $B2$ local structure even far from stoichiometry, [19,31] amorphous Fe$_x$Si$_{1-x}$ samples behave very differently as they lose the short- and long-range orderings. Very recently, Karel *et al.* [31] have showed that amorphous Fe$_x$Si$_{1-x}$ samples ($0.58 < x < 0.68$) have significantly enhanced spin polarization, up to 70% at $x = 0.65$ measured by Andreev reflection spectroscopy [32], a value which is much larger than the corresponding value in the ordered phase (49%).

In the present work, we systematically investigated the electronic structures, magnetic and magneto-optic properties of $D0_3$-Fe$_3$Si, as well as the modifications of these properties caused by the structure disordering. Compared with the $D0_3$-Fe$_3$Si, we found that the amorphous Fe$_3$Si has larger average magnetic moment and broader band. Furthermore, the structural disordering has an insignificant influence on the anomalous Hall conductivity around the Fermi level but noticeably affects the magneto-optical Kerr rotation spectrum. These results provide a comprehensive collection of physical properties of Fe$_x$Si$_{1-x}$ alloys around the concentration of $x = 0.75$ and shed light for the control and optimization of spintronic performance of intermetallic alloys.

II. MODELS AND METHOD

The first-principles calculations were performed using the projector augmented wave method (PAW) as implemented in the Vienna *Ab initio* Simulation Package (VASP). The exchange-correlation interactions were described by the generalized-gradient approximation with the Perdew-Burke-Ernzerhof functional [33]. An energy cutoff of 350 eV was

*Corresponding author: yanningz@uestc.edu.cn
†Corresponding author: wur@uci.edu
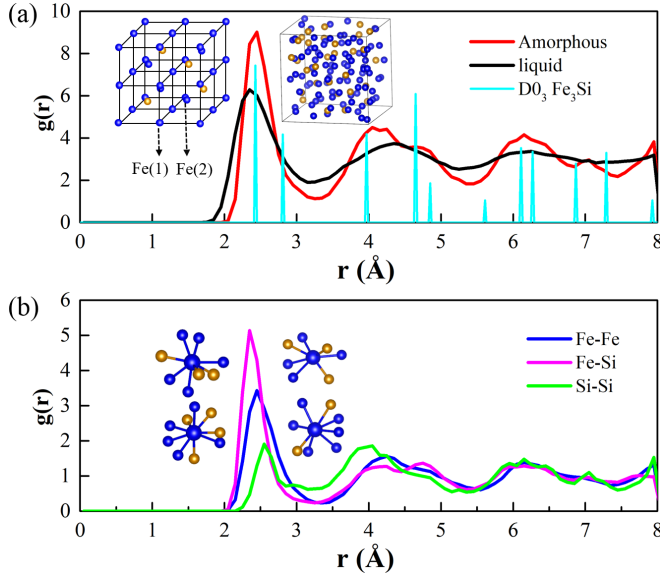
FIG. 1. The partial pair-distribution function for (a) $D0_3$, liquid and amorphous Fe_3Si. The left and right insets depict the $D0_3$ and amorphous structures with blue and brown balls for Fe and Si atoms, respectively (b) Fe-Fe, Fe-Si, Si-Si pair-distribution functions in amorphous Fe_3Si. The four configurations in insets are the most typical local configurations at the first PDF peak with the central Fe atom and its neighbors within a range of 2.6 Å.

used for the plane-wave basis expansion. All atoms were fully relaxed using the conjugate gradient method until the force acting on each atom was less than 0.01 eV/Å.

The $D0_3$-Fe_3Si is a quasi-Heusler compound in the chemically ordered phase with two inequivalent Fe lattice sites, as shown in the left inset in Fig. 1(a). While one Fe site is surrounded by four nearest Fe atoms and four nearest Si atoms [denoted as Fe(1)], the other Fe site is surrounded by eight nearest Fe atoms [denoted as Fe(2)]. The Brillouin zone was sampled with a $12 \times 12 \times 12$ Monkhorst-Pack k-point mesh. The optimized lattice constant, $a = 5.61$ Å, is consistent with the experimental value of 5.65 Å [34].

In order to obtain the amorphous Fe_3Si structure, we performed *ab initio* molecular dynamics (AIMD) simulations in a $4 \times 4 \times 4$ supercell with 128 atoms. The initial configuration was prepared by randomly distributing Fe and Si atoms on the lattice sites in a ratio of 3:1. The system is then gradually heated up to 3000 K in 10 ps and annealed at 3000 K for 4 ps to get a fully molten liquid state. Afterwards, we cooled the system down to 100 K in 6 ps to get the amorphous structure. Only the Γ point was used in the AIMD simulations. After that, a $3 \times 3 \times 3$ Monkhorst-Pack k-point mesh was adopted for the further structural optimization and finally for the determination of electronic and magnetic properties of amorphous Fe_3Si, as depicted in the right inset in Fig. 1(a).

III. RESULTS

A. Molecular dynamics simulations for amorphous Fe_3Si

The pair-distribution function [PDF, $g(r)$] is a very important quantity for studies of liquid and amorphous structures. The PDF describes the density of atoms at a distance from

the reference atom and characterizes the degree of structural disordering. The PDF [35] can be obtained as

$$g(r) = \frac{V}{N}\left(\frac{n(r, \Delta r)}{4\pi r^2 \Delta r}\right). \quad (1)$$

Here, V is the volume of simulation system, N is the number of atoms, and $n(r, \Delta r)$ is the number of atoms around a central atom within the interval between r and $r + \Delta r$. The PDF of the quenched Fe_3Si system is shown in Fig. 1(a), together with those of the crystalline and liquid Fe_3Si structures. While the black and red lines overall follow each other, the two shoulders of the second peak around the cyan spikes clearly imply the formation of the amorphous structure, as have been observed for many amorphous materials such as $Fe_{78}Si_9B_{13}$ alloys [36].

Furthermore, we show its partial PDF of Fe-Fe, Fe-Si, and Si-Si pairs in Fig. 1(b). Clearly, $g_{Fe-Si}(r)$ has the highest first peak, indicating that Fe is more likely to bind with its surrounding Si atoms. The first peak of $g_{Fe-Si}(r)$ locates at about 2.35 Å, which means that the average nearest-neighbor distance of Fe-Si pairs is shorter than the corresponding Fe–Fe and Fe–Si bonds in $D0_3$-Fe_3Si ($\sim$2.43 Å) by 3.3%. The $g_{Si-Si}(r)$ curve has the lowest first peak but a relatively high second peak around 4.0 Å. This characteristic indicates that Si atoms avoid forming the first neighbors as they are slightly ionized by Fe atoms in FeSi alloys.

B. Electronic and magnetic properties

To investigate the influence of structure disordering on the electronic and magnetic properties of Fe_3Si, we present the magnetic moment distribution in Fig. 2(a). For the $D0_3$ Fe_3Si (two red columns with shadow), the local magnetic moments of Fe atoms depend strongly on their environment. The Fe atoms surrounded by four Fe atoms and four Si atoms have a low magnetic moment of $M[Fe(1)] = 1.32\,\mu_B$, whereas the other four Fe atoms which have all eight Fe neighbors have a high magnetic moment of $M[Fe(2)] = 2.52\,\mu_B$. This difference can also be seen in Fig. 2(b) by the curves of projected density of states (PDOS), a quantity which weights the contribution from each individual atom by integrating the wave functions in a designated spatial region (e.g., a sphere) or by projecting the wave functions to atomic orbitals or spherical harmonics. While there is a broad peak of Fe(1)-d states in the minority spin channels at the Fermi level (E_F), Fe(2)-d orbitals near E_F in the minority spin channel obviously split, in good agreement with previous studies [37].

In contrast, the PDOS profiles are broadened significantly in the amorphous Fe_3Si. The magnetic moment distribution in amorphous Fe_3Si becomes widely spread, as shown by black columns in Fig. 2(a). The average magnetization (i.e., the total magnetic moment divided by the total number of Fe and Si atoms) is $1.37\,\mu_B$/atom, obviously larger than that of the crystalline $D0_3$-Fe_3Si, $1.28\,\mu_B$/atom. The analyses on the local surroundings of different Fe atoms show that the local magnetic moment of Fe increases with the decrease of their neighboring atoms, particularly Si. For example, the Fe atom with the smallest magnetization, $\sim$0.4 μ_B, is surrounded by nine atoms, five Si and four Fe, whereas the Fe atom with the largest magnetic moment, $\sim$2.4 μ_B, is surrounded by only
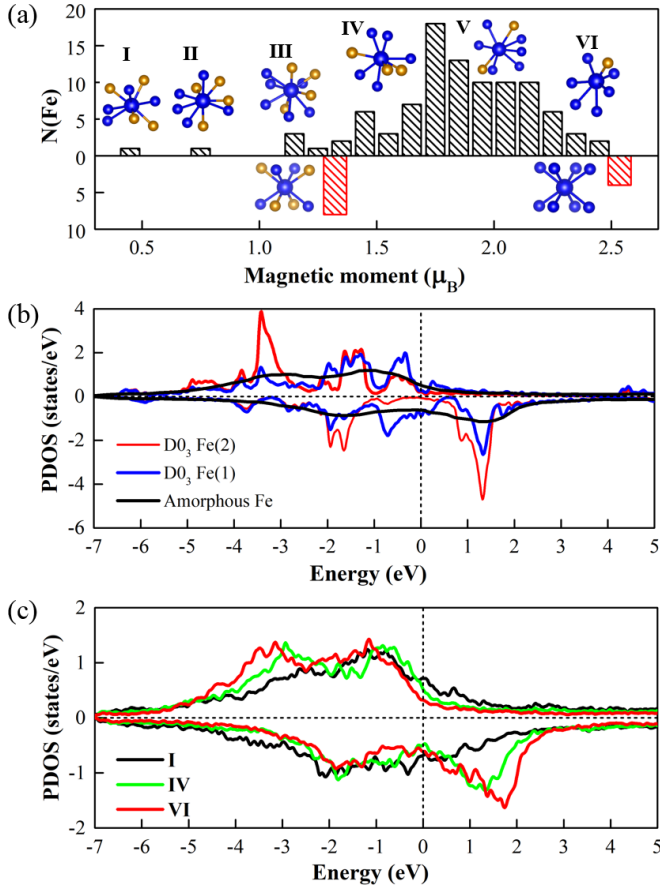
FIG. 2. (a) The number of Fe atoms within a range of magnetic moment ($M \pm 0.05 \, \mu_B$) in amorphous Fe$_3$Si, and insets show a few corresponding local configurations with neighbors around those Fe atoms within a range of 2.6 Å. The Fe and Si atoms in insets are represented by blue and brown balls, respectively. (b) The PDOS of Fe atoms in the $D0_3$ Fe$_3$Si and averaged PDOS per Fe atom in the amorphous Fe$_3$Si. (c) The PDOS of Fe atoms in the amorphous Fe$_3$Si, corresponding to configurations I, IV, and VI in (a), respectively.

seven atoms, one Si and six Fe. At this concentration, all Fe atoms in amorphous Fe$_3$Si have Si neighbors, causing the disappearance of Fe(2)-type atoms as in the crystalline structure. The PDOS curves of several representative Fe atoms, i.e., those with the smallest, intermediate, and the largest magnetic moments, in the amorphous Fe$_3$Si are shown in Fig. 2(c). It is apparent that the profiles of PDOS curves correlate with the magnetic moments of Fe atoms. For Fe atoms with large magnetic moment (type VI), the d bands are broad and the exchange splittings are more obvious. As they gain some electrons from Si and mostly Fe neighbors, the spin-up bands are almost fully occupied, and the separation between bonding-antibonding peaks in the spin-down channel is more obvious. In contrast, the PDOS curves of Fe atoms with smaller magnetic moment are narrower, and their exchange splittings are also smaller, due to the presence of nonbonding states around the Fermi level because the hybridization between Fe and nonmagnetic Si is weaker than Fe-Fe hybridization. The Bader charge analyses indicate that each Si atom transfers 0.19 e to its Fe neighbors in the amorphous phase.

C. Anomalous Hall effect

In Figs. 2(b) and 2(c), the modifications of electronic and magnetic properties by the structural disordering can be found in the entire energy range, particularly near the Fermi level. Therefore, transport properties such as the spin polarization and the anomalous Hall effect (AHE) are expected to be strongly altered. In previous studies, we addressed the enhanced spin polarization in amorphous Fe$_x$Si$_{1-x}$ for carriers near the Fermi level [19,31]. From the curves of PDOS in Figs. 2(b) and 2(c), we may attribute this enhancement to the appearance of type-VI Fe atoms and Si→Fe charge transfer in the amorphous environment. Here, we focus on studying another important transport property: the intrinsic anomalous Hall conductivity (AHC). In general, the anomalous Hall effect in a ferromagnet may also be affected by extrinsic mechanisms such as skew and side-jump scatterings. The intrinsic AHE from the electronic band structures nevertheless plays the dominate role in most materials [38], and hence we only consider the intrinsic part in this work.

The intrinsic anomalous Hall conductivity σ_{xy} is calculated by integrating the Berry curvature over the Brillouin zone [39]:

$$\sigma_{xy} = -\frac{e^2}{h} \int_{\text{BZ}} \frac{d^3k}{(2\pi)^3} \Omega^z(k), \tag{2}$$

where $\Omega^z(k)$ is determined as [39]

$$\Omega^z(k) = \sum_n f_n \Omega_n^z(k)$$

$$= -\sum_{n,m \neq n} f_n(k) \frac{2\text{Im}\langle \psi_{nk}|v_x|\psi_{mk}\rangle \langle \psi_{mk}|v_y|\psi_{nk}\rangle}{(\omega_m - \omega_n)^2}. \tag{3}$$

Here, f_n is the Fermi occupation factor, ψ_{nk} and $E_n = \hbar\omega_n$ are the spinor Bloch wave function and eigenvalue of the nth band at a k point, and v_x, v_y are velocity operators.

The calculated AHC of the $D0_3$-Fe$_3$Si at room temperature is 237 $(\Omega \, \text{cm})^{-1}$, which is smaller than the value of the bulk body-centered cubic Fe [39]. The AHC is mainly attributed to the large Berry curvature in the vicinity around $2/3(\Gamma$-$M)$ in the Brillouin zone as shown in Fig. 3(a). The spin-resolved band structure of $D0_3$-Fe$_3$Si, with the spin-orbit coupling (SOC) included, is shown in Fig. 3(b). To highlight the effect of SOC, different colors are used to indicate the mixing ratio of spin-up (blue) and spin-down (red) components. We found that the large Berry curvature results from spin-down d_{xz}/d_{yz} states that interact across the Fermi energy, as marked by a black circle in Fig. 3(b). The small SOC-induced energy splitting gives rise to small denominators in Eq. (3), and hence produces a large peak of Berry curvature in the Brillouin zone.

For the amorphous Fe$_3$Si, the room-temperature AHC is 222 $(\Omega \, \text{cm})^{-1}$, a value that is similar with that of $D0_3$ Fe$_3$Si. This is not surprising because the total DOS of amorphous Fe$_3$Si near the Fermi energy does not change much compared with that of $D0_3$ Fe$_3$Si. However, AHCs of the crystalline and amorphous phases behave very differently as we shift the position of the Fermi level according to a rigid-band model, as shown in Fig. 3(c). For $D0_3$-Fe$_3$Si, the AHC can reach a maximum of 1127 $(\Omega \, \text{cm})^{-1}$ when the Fermi level is lowered
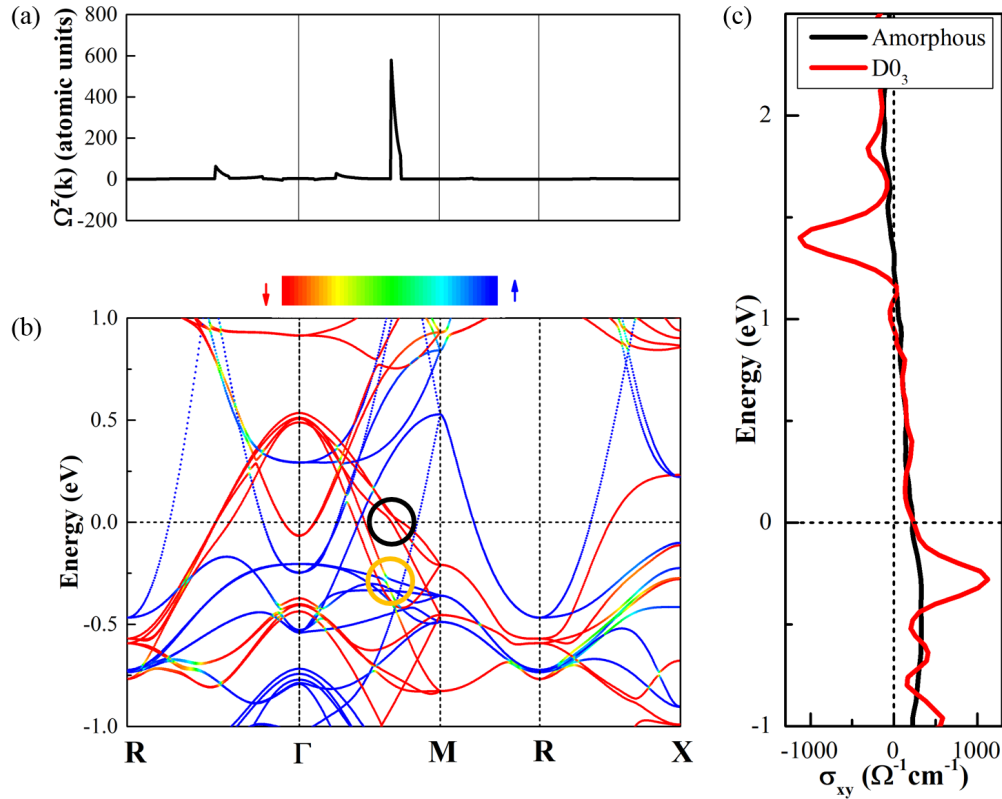
FIG. 3. (a) Berry curvature and (b) spin-resolved band structure of the $D0_3$-Fe$_3$Si along the high-symmetric path R-Γ-M-R-X in the Brillouin zone. The color bar indicates the mixing ratio of two spins. (c) The AHC as a function of the Fermi level according to a rigid-band model.

by -0.28 eV, which suggests the potential of manipulating AHC in a large range by doping or gating. This large value is attributed to the SOC between a pair of spin-up/spin-down bands around $1/2(\Gamma$-$M)$ in the Brillouin zone, as marked by an orange circle in Fig. 3(b). The bands in green color contribute the most since the green color indicates a strong intermix of two spin components, which usually produces a large Berry curvature. Overall, the AHC of amorphous Fe$_3$Si varies slowly and smoothly with the change of the Fermi level due to the broadened DOS profile, whereas AHC of crystalline Fe$_3$Si has more features. We tested several different initial configurations for the MD simulations and found that the values of AHC may vary slightly within a range of $\sim$5%.

We want to emphasize that the AHC of amorphous Fe$_3$Si was calculated with a supercell according to Eqs. (2) and (3). One may argue that the Brillouin zone disappears as the supercell expands to infinity and this approach may become questionable. We perceive that the SOC information is carried over by electronic states no matter how many times we fold the Brillouin zone. Even though bands eventually become energy levels, Eq. (3) is still applicable whereas the integral in Eq. (2) becomes unnecessary as the Brillouin zone shrinks to a dot. As amorphous materials have varying local atomic configurations in different spatial regions, the sharp peaks in the $\sigma_{xy}(E - E_F)$ spectrum due to the quasidegeneracy of bands in ordered structure disappear. Nonetheless, the almost unaffected main parts indicate that contributions to AHC from

pairs of states with finite energy separations are insensitive to the change of environment.

D. The magneto-optical Kerr effect

Magneto-optical Kerr spectroscopy is a useful technique for studies of magnetic systems via the polarization and energy-dependent reflection and absorption. In a polar geometry, where the z axis is chosen to be parallel to the magnetization direction, the complex Kerr angle is given by [40]

$$\phi_K \equiv \phi_K + i\varepsilon_K = \frac{-\sigma_{xy}}{\sigma_{xx}\sqrt{1 + i\left(\frac{4\pi}{\omega}\right)\sigma_{xx}}}, \quad (4)$$

where ϕ_K is the real Kerr rotation angle, ε_K stands for the Kerr ellipticity, σ_{xx} and σ_{xy} are components of the conductivity tensor calculated by using the Kubo formula:

$$\sigma_{\alpha\beta}(\omega) = \frac{ie^2}{Vm^2\hbar} \sum_{\boldsymbol{k}} \sum_{m,n} \frac{f_m(\boldsymbol{k}) - f_n(\boldsymbol{k})}{\omega_{mn}(\boldsymbol{k})} \frac{p_{mn}^{\alpha}(\boldsymbol{k})p_{nm}^{\beta}(\boldsymbol{k})}{\omega - \omega_{mn}(\boldsymbol{k}) + i\eta}. \quad (5)$$

Here, V is the volume of the unit cell, $f_n(\mathbf{k})$ is the Fermi occupation factor of the nth eigenstate at wave vector $\mathbf{k}$. $\hbar\omega_{mn}(\mathbf{k}) = E_m(\mathbf{k}) - E_n(\mathbf{k})$ is the energy difference between the mth and nth states, $\hbar\omega$ is the incident phonon energy, and $p_{nm}^{\alpha}(\mathbf{k})$ is the matrix element of the momentum operator. The
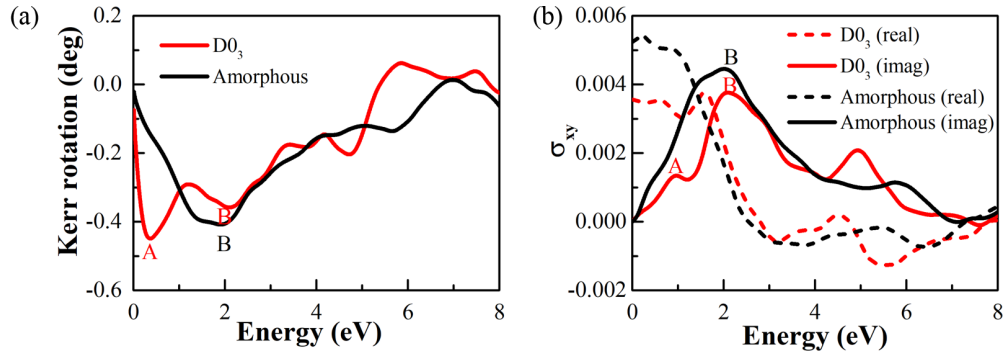
FIG. 4. The (a) Kerr rotation angle and (b) conductivity tensor σ_{xy} of $D0_3$ and amorphous Fe_3Si.

lifetime effect of the excited Bloch states is taken into account by setting a broadening of $\eta = 0.3$ eV [40].

The magneto-optical Kerr rotation angle as a function of photon energy for both $D0_3$ and amorphous Fe_3Si are plotted in Fig. 4(a). There are two noticeable peaks (large Kerr rotation) for the $D0_3$ structure, locating at 0.37 eV (denoted as peak A) and 2.09 eV (denoted as peak B), respectively. Instead, the peak A completely disappears when the structure becomes disordered, whereas the position of peak B is almost unchanged with a stronger intensity. The plotted conductivity tensor σ_{xy} in Fig. 4(b) clearly shows that the Kerr rotation mainly follows the trend of the imaginary part of σ_{xy}.

To understand the change of the optical conductivity curve and further the Kerr rotation spectra, we resolve the imaginary part of σ_{xy} at a specified photon energy to contributions from different slices in the Brillouin zone by

$$\sigma_{xy}(\mathbf{k}_z) = \sum_{k_x, k_y} \sigma_{xy}. \qquad (6)$$

The $k_{x,y}$-integrated σ_{xy} values of the $D0_3$-Fe_3Si as a function of k_z are shown in Fig. 5(a). Since $\sigma_{xy}(\mathbf{k}_z) = \sigma_{xy}(-\mathbf{k}_z)$, only contributions of $\mathbf{k}_z > 0$ are presented. It is shown that the peak A is mainly contributed by states at the planes of
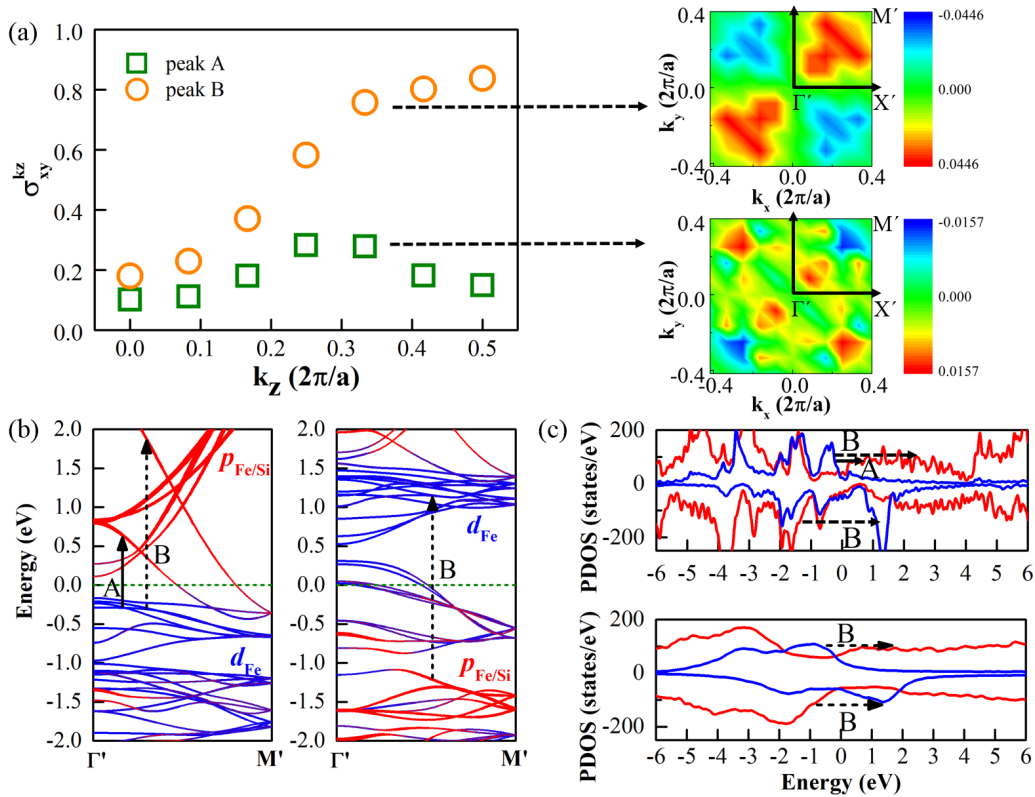
FIG. 5. (a) Left: The contribution to the imaginary part of σ_{xy} of each $\mathbf{k}_z$ plane in the Brillouin zone for $D0_3$ Fe_3Si. Right: The distribution of the imaginary part of σ_{xy} in $\mathbf{k}_z = 1/3$ plane, where the red and blue represents positive and negative contributions, respectively. (b) The band structure of $D0_3$ Fe_3Si without SOC along $\Gamma' = (0, 0, 1/3)$ to $M' = (1/2, 1/2, 1/3)$. The p states and d states are represented by red and blue lines, respectively, and the linewidth scales with their weights. For clarity the p states are enlarged by a factor of 10. The dominate interband transitions of peak A and B are marked by solid and dashed lines, respectively. (c) The projected DOS of $D0_3$ (up panel) and amorphous (down panel) Fe_3Si. The p states and d states are represented by red and blue lines, respectively, and the p states are enlarged by a factor of 20.

$\mathbf{k}_z$ = 1/3, 5/12, 1/2, and the peak B is mainly contributed by states at the planes of $\mathbf{k}_z$ = 1/4 and 1/3, as scaled by the length $\mathbf{k}_z$ in the first Brillouin zone. We further show the distribution of imaginary part of σ_{xy} in the $k_{x,y}$ plane at $\mathbf{k}_z$ = 1/3 by contour plots in the right panels of Fig. 5(a), where the red and blue areas represent positive and negative contributions, respectively. The most eye-catching region is around 1/6(Γ'-M') for the peak A, and around 1/2(Γ'-M') for the peak B, where Γ' = (0, 0, 1/3), M' = (1/2, 1/2, 1/3). As a further step, we analyzed the band structure of $D0_3$-Fe$_3$Si along the Γ'-M' line and identified the dominant interband transitions that contribute to the conductivity peaks from the momentum matrix elements. Although the Kerr rotation was calculated with SOC, for a better clarity we mark the transitions by arrows on the spin-up and spin-down band structures. It is found from Fig. 5(b) that the peak A is mainly contributed by transitions from the occupied Fe-d states (d_{Fe}) just below E_F to the unoccupied hybrid Fe/Si-p states ($p_{Fe/Si}$) at 0.65 eV in the spin-up channel. The interband transitions produce the peak B from two parts: the occupied d_{Fe} to unoccupied $p_{Fe/Si}$ in the spin-up channel and $p_{Fe/Si}$ at a deep energy of -1.25 eV to d_{Fe} at 1.2 eV in the spin-down channel.

The interband matrix analysis for the amorphous Fe$_3$Si is rather complicated. Instead, we calculated the p/d projected DOS as shown in Fig. 5(c). For clarity and easy comparison, the DOS curves of p states are enlarged by a factor of 10. Compared with the DOS of $D0_3$-Fe$_3$Si, a significant change is that the occupied d states around -0.3 eV vanish in the amorphous structure, which results in the disappearance of peak A as shown in Figs. 4(a) and 4(b). Again, the bands are folded to energy levels as the Brillouin zone shrinks for the amorphous structures, and the optical response takes contributions from different regions and hence the sharp features disappear.

IV. CONCLUSIONS

Through extensive density-functional calculations, we investigated the electronic, magnetic, transport, and magneto-optical properties of the $D0_3$ and amorphous Fe$_3$Si. Pair-correlation function analyses for the amorphous Fe$_3$Si obtained by AIMD simulations showed that Si atoms prefer to bond with Fe atoms in the amorphous structure. The increase of Si neighbors purges the magnetization of Fe, while a small number of Si neighbors is beneficial for the enhancement of spin polarization at the Fermi level because of Si $\rightarrow$ Fe charge transfer. The structural disordering significantly alters magneto-optical Kerr effect, but not as strong on the anomalous Hall effect. The intrinsic AHC of $D0_3$-Fe$_3$Si is $237\,(\Omega\,\mathrm{cm})^{-1}$ at room temperature and can be tuned to a high value of $1127\,(\Omega\,\mathrm{cm})^{-1}$ when the Fermi energy is lowered by -0.28 eV. In contrast, the AHC of amorphous Fe$_3$Si varies slowly with the shift of the Fermi level, indicating that it is insensitive to doping or gating. The Kerr rotation angle shows two main peaks in the energy range of 0~4 eV for the $D0_3$-Fe$_3$Si, whereas the first peak disappears when the structure becomes disordered. Our studies provide comprehensive data for FeSi alloys around this concentration ratio and the overall physical insights should be useful for the design of amorphous spintronic materials.

[1] M. C. Bost and J. E. Mahan, J. Appl. Phys. **58**, 2696 (1985).

[2] N. E. Christensen, Phys. Rev. B **42**, 7148 (1990).

[3] D. Leong, M. Harry, K. J. Reeson, and K. P. Homewood, Nature (London) **387**, 686 (1997).

[4] V. Jaccarino, G. K. Wertheim, J. H. Wernick, L. R. Walker, and S. Arajs, Phys. Rev. **160**, 476 (1967).

[5] Z. Schlesinger, Z. Fisk, H.-T. Zhang, M. B. Maple, J. F. DiTusa, and G. Aeppli, Phys. Rev. Lett. **71**, 1748 (1993).

[6] C. Fu, M. P. C. M. Krijn, and S. Doniach, Phys. Rev. B **49**, 2219(R) (1994).

[7] K. Seo, S. Lee, Y. Jo, M. H. Jung, J. Kim, D. G. Churchill, and B. Kim, J. Phys. Chem. C **113**, 6902 (2009).

[8] W. A. Hines, A. H. Menotti, J. I. Budnick, T. J. Burch, T. Litrenta, V. Niculescu, and K. Raj, Phys. Rev. B **13**, 4060 (1976).

[9] J. Kudrnovský, N. E. Christensen, and O. K. Andersen, Phys. Rev. B **43**, 5924 (1991).

[10] E. G. Moroni, W. Wolf, J. Hafner, and R. Podloucky, Phys. Rev. B **59**, 12860 (1999).

[11] A. Ionescu, C. A. F. Vaz, T. Trypiniotis, C. M. Gürtler, H. García-Miquel, J. A. C. Bland, M. E. Vickers, R. M. Dalgliesh, S. Langridge, Y. Bugoslavsky, Y. Miyoshi, L. F. Cohen, and K. R. A. Ziebeck, Phys. Rev. B **71**, 094401 (2005).

[12] J. Herfort, H. P. Schonherr, and K. H. Ploog, Appl. Phys. Lett. **83**, 3912 (2003).

[13] A. Kawaharazuka, M. Ramsteiner, J. Herfort, H. P. Schönherr, H. Kostial, and K. H. Ploog, Appl. Phys. Lett. **85**, 3492 (2004).

[14] T. Sunohara, K. I. Kobayashi, M. Umada, H. Yanagihara, E. Kita, H. Akinaga, and T. Suemasu, Jpn. J. Appl. Phys. **44**, L715 (2005).

[15] F. Lin, D. Jiang, X. Ma, and W. Shi, Thin Solid Films **515**, 5353 (2007).

[16] K. Ueda, M. Kumano, T. Sadoh, and M. Miyao, Thin Solid Films **517**, 425 (2008).

[17] K. Ueda, T. Sadoh, Y. Ando, T. Jonishi, K. Narumi, Y. Maeda, and M. Miyao, Thin Solid Films **517**, 422 (2008).

[18] S. Yamada, J. Sagar, S. Honda, L. Lari, G. Takemoto, H. Itoh, A. Hirohata, K. Mibu, M. Miyao, and K. Hamaya, Phys. Rev. B **86**, 174406 (2012).

[19] Kh. Zakeri, I. Barsukov, N. K. Utochkina, F. M. Römer, J. Lindner, R. Meckenstock, U. von Hörsten, H. Wende, W. Keune, M. Farle, S. S. Kalarickal, K. Lenz, and Z. Frait, Phys. Rev. B **76**, 214421 (2007).

[20] B. Krumme, C. Weis, H. C. Herper, F. Stromberg, C. Antoniak, A. Warland, E. Schuster, P. Srivastava, M. Walterfang, K. Fauth, J. Minár, H. Ebert, P. Entel, W. Keune, and H. Wende, Phys. Rev. B **80**, 144403 (2009).

[21] K. Kasahara, S. Yamada, K. Sawano, M. Miyao, and K. Hamaya, Phys. Rev. B **84**, 205301 (2011).

[22] L. L. Tao, S. H. Liang, D. P. Liu, H. X. Wei, J. Wang, and X. F. Han, Appl. Phys. Lett. **104**, 172406 (2014).

[23] K. Lenz, E. Kosubek, K. Baberschke, H. Wende, J. Herfort, H. P. Schönherr, and K. H. Ploog, Phys. Rev. B **72**, 144411 (2005).

[24] Y. Ando, K. Hamaya, K. Kasahara, K. Ueda, Y. Nozaki, T. Sadoh, Y. Maeda, K. Matsuyama, and M. Miyao, J. Appl. Phys. **105**, 07B102 (2009).

[25] Y. N. Zhang, J. X. Cao, I. Barsukov, J. Lindner, B. Krumme, H. Wende, and R. Q. Wu, Phys. Rev. B **81**, 144418 (2010).

[26] M. Bowen, K.-J. Friedland, J. Herfort, H. P. Schönherr, and K. H. Ploog, Phys. Rev. B **71**, 172401 (2005).

[27] P. K. Muduli, K.-J. Friedland, J. Herfort, H. P. Schönherr, and K. H. Ploog, Phys. Rev. B **72**, 104430 (2005).

[28] B. L. Guo, P. Li, C. Jin, H. Liu, and H. L. Bai, Phys. Status Solidi B **251**, 761 (2014).

[29] T. J. Burch, T. Litrenta, and J. I. Budnick, Phys. Rev. Lett. **33**, 421 (1974).

[30] K. Hamaya, H. Itoh, O. Nakatsuka, K. Ueda, K. Yamamoto, M. Itakura, T. Taniyama, T. Ono, and M. Miyao, Phys. Rev. Lett. **102**, 137204 (2009).

[31] J. Karel, Y. N. Zhang, C. Bordel, K. H. Stone, T. Y. Chen, C. A. Jenkins, D. J. Smith, J. Hu, R. Q. Wu, S. M. Heald, J. B. Kortright, and F. Hellman, Mater. Res. Express **1**, 026102 (2014).

[32] J. Karel, D. S. Bouma, J. Martinez, Y. N. Zhang, J. A. Gifford, J. Zhang, G. J. Zhao, D. R. Kim, B. C. Li, Z. Y. Huang, R. Q. Wu, T. Y. Chen, and F. Hellman, Phys. Rev. Mater. **2**, 064411 (2018).

[33] J. P. Perdew, K. Burke, and M. Ernzerhof, Phys. Rev. Lett. **77**, 3865 (1996).

[34] D. Odkhuu and S. C. Hong, IEEE Trans. Magn. **47**, 2920 (2011).

[35] C. Y. Liu, F. Wang, F. F. Rao, Y. S. Hou, S. Y. Wang, Q. Sun, and Y. Jia, J. Appl. Phys. **113**, 154306 (2013).

[36] T. K. Gu, J. Y. Qin, and X. F. Bian, Appl. Phys. Lett. **91**, 081907 (2007).

[37] M. Ležaić, P. Mavropoulos, S. Blügel, and H. Ebert, Phys. Rev. B **83**, 094434 (2011).

[38] J. Karel, C. Bordel, D. S. Bouma, A. de Lorimier-Farmer, H. J. Lee, and F. Hellman, EPL **114**, 57004 (2016).

[39] Y. Yao, L. Kleinman, A. H. MacDonald, J. Sinova, T. Jungwirth, D.-s. Wang, E. Wang, and Q. Niu, Phys. Rev. Lett. **92**, 037204 (2004).

[40] P. M. Oppeneer, T. Maurer, J. Sticht, and J. Kübler, Phys. Rev. B **45**, 10924 (1992).